Rock Mech Rock Eng (2016) 49:1497–1515
DOI 10.1007/s00603-015-0838-3

ORIGINAL PAPER

An Experimental and Numerical Study on Cracking Behavior of Brittle Sandstone Containing Two Non-coplanar Fissures Under Uniaxial Compression

Sheng-Qi Yang[1] · Wen-Ling Tian[1] · Yan-Hua Huang[1] · P. G. Ranjith[2] · Yang Ju[1,3]

Received: 7 April 2015 / Accepted: 2 September 2015 / Published online: 12 September 2015

Abstract To understand the fracture mechanism in all kinds of rock engineering, it is important to investigate the fracture evolution behavior of pre-fissured rock. In this research, we conducted uniaxial compression experiments to evaluate the influence of ligament angle on the strength, deformability, and fracture coalescence behavior of rectangular prismatic specimens (80 × 160 × 30 mm) of brittle sandstone containing two non-coplanar fissures. The experimental results show that the peak strength of sandstone containing two non-coplanar fissures depends on the ligament angle, but the elastic modulus is not closely related to the ligament angle. With the increase of ligament angle, the peak strength decreased at a ligament angle of 60°, before increasing up to our maximum ligament angle of 120°. Crack initiation, propagation, and coalescence were all observed and characterized from the inner and outer tips of pre-existing non-coplanar fissures using photographic monitoring. Based on the results, the sequence of crack evolution in sandstone containing two non-coplanar fissures was analyzed in detail. In order to fully understand the crack evolution mechanism of brittle sandstone, numerical simulations using PFC^{2D} were performed for specimens containing two non-coplanar fissures under uniaxial compression. The results are in good agreement with the experimental results. By analyzing the stress field, the crack evolution mechanism in brittle sandstone containing two non-coplanar fissures under uniaxial compression is revealed. These experimental and numerical results are expected to improve the understanding of the unstable fracture mechanism of fissured rock engineering structures.

Keywords Brittle sandstone · Two non-coplanar fissures · Crack initiation · Crack coalescence · Tensile crack

✉ Sheng-Qi Yang
yangsqi@hotmail.com

[1] State Key Laboratory for Geomechanics and Deep Underground Engineering, China University of Mining and Technology, Xuzhou 221116, China

[2] Deep Earth Energy Research Laboratory, Department of Civil Engineering, Monash University, Melbourne, VIC 3800, Australia

[3] State Key Laboratory of Coal Resources and Safe Mining, China University of Mining Technology, Beijing 100083, China

1 Introduction

Rock is a kind of natural geological material, which usually includes unequal flaws with different shapes (such as holes, fissures, inclusions) (Debecker and Vervoort 2009; Feng et al. 2009; Hall et al. 2006; Janeiro and Einstein 2010; Park and Bobet 2009; Prudencio and Van Sint Jan 2007; Yang and Jing 2011). In order to understand the fracture mechanism of rock engineering, many experimental and numerical investigations have been carried out on rocks containing various fissures (Lee and Jeon 2011; Li et al. 2005; Mughieda and Omar 2008; Vásárhelyi and Bobet 2000; Wong and Einstein 2009; Yang et al. 2012), which show that pre-existing fissures in natural rock masses have a great influence on their strength, deformation, and fracture coalescence behavior (Hall et al. 2006; Lee and Jeon 2011; Li et al. 2005; Yang and Huang 2014; Yang et al. 2014).

Hall et al. (2006) carried out an experimental study on natural and dry specimens of Neapolitan fine-grained tuff, and analyzed the crack coalescence processes of specimens containing one and two pre-existing fissures using acoustic emission (AE) and photographic monitoring, which were

helpful to predict sudden and unexpected collapses of underground rock engineering. Wong and Einstein (2009) studied experimentally the crack coalescence behavior of Carrara marble specimens containing two pre-existing fissures and summarized the influence of the different fissure geometries on the cracking processes. Esterhuizen et al. (2011) analyzed the coalescence of two inclined discontinuities in a partially benched pillar (with a width-to-height ratio of 0.58) containing a macroscopic fracture. Lee and Jeon (2011) carried out uniaxial compression tests on Hwangdeung granite containing two unparallel fissures and analyzed the crack initiation and propagation patterns, which were distinctly different from those containing two parallel fissures (Wong and Einstein 2009). Yang (2011) conducted an experimental investigation of brittle sandstone specimens containing two coplanar fissures and characterized the effect of coplanar fissure angle on the crack coalescence process and type of brittle sandstone material using photographic monitoring techniques.

With the development of numerical methods, many simulation softwares have been adopted to analyze the crack coalescence processes of real rock material, including SAP2000 (Mughieda and Omar 2008), FROCK (Vásárhelyi and Bobet 2000), PFC^{2D} (Lee and Jeon 2011; Yang and Huang 2014; Yang et al. 2014), RFPA^{2D} (Tang 1997; Tang et al. 1997), the boundary element method (BEM) (Chen et al. 1998; Shen and Stephansson 1993; Shen 1995), cellular automata (CA) (Feng et al. 2006; Pan et al. 2009), and X-FEM (Colombo and Massin 2011; Grégoire et al. 2007; Rozycki et al. 2008). Mughieda and Omar (2008) investigated the stress distribution of rock containing two fissures using the finite element code SAP2000. The simulated results showed that tensile stress was mainly responsible for wing crack initiation, while shear stress was responsible for secondary crack initiation. Vásárhelyi and Bobet (2000) adopted FROCK software to model experimental observations of pre-cracked specimens of gypsum. They analyzed the crack initiation stress, the direction and propagation of the new cracks, and the type of coalescence in gypsum containing two open and closed fissures. RFPA^{2D} (a rock failure process analysis code) was developed by Northeastern University, China (Tang 1997; Tang et al. 1997), which can reproduce many conventional phenomena of rock mechanics in the laboratory (Tang and Kou 1998; Tang et al. 2000). Wong et al. (2002) analyzed crack growth in brittle rocks containing a single, triple, and multiple fissures under uniaxial compression using RFPA^{2D} and found that the fissure length, fissure location, and stress interactions between the nearby fissures are important factors affecting crack initiation, propagation, and coalescence behaviors. Using PFC^{2D} based on the discrete element method (DEM), Lee and Jeon (2011) carried out a numerical simulation of the crack coalescence characteristics in Hwangdeung granite containing two unparallel fissures, and the results showed good agreement with the experimental results.

However, in real rock engineering practice, non-coplanar fissures exist, which are likely to coalesce with pre-existing fissures along the ligament region under complex stress states. Once the coalescence between two fissures occurs, the rock mass will likely suffer unstable failure. However, in previous studies, few experiments and numerical simulations have been carried out on real rock specimens containing two non-coplanar fissures, and the fracture coalescence mechanism of rock material containing two non-coplanar fissures is little understood. Therefore, the main aim of this research is to analyze the strength and deformation behavior of brittle sandstone specimens containing two non-coplanar fissures and to investigate the fracture coalescence process by experiment and numerical simulation.

2 Rock Specimens and Testing Procedure

To study the fracture coalescence behavior of brittle rock containing two non-coplanar fissures under uniaxial compression, sandstone from Linyi City, Shandong province, China, was chosen for testing. The mineral components of the sandstone specimens are feldspar, quartz, and debris (Fig. 1), which are the same as in a previous study (Yang 2011). The tested sandstone has a crystalline and blocky structure with a porosity of about 4.61 %, which is a fine-grained heterogeneous material with an average unit weight of about 2650 kg/m^3. A more detailed description of the tested material can be found in Yang (2011).

The size of the tested sandstone specimens was approximately 80 × 160 × 30 mm. The geometry of the sandstone specimens with two non-coplanar fissures is described in Fig. 2. It should be noted that the terms "fissure" and "crack" are very different, a fissure being defined as an artificially created flaw, but a crack is described as a new fracture or failure during loading (Yang 2011). The geometry of two non-coplanar fissures is defined by four geometric parameters: fissure length $2a$, ligament length $2b$, fissure angle (the angle of the fissure with the horizontal direction) α, and ligament angle β, as shown in Fig. 2.

Two non-coplanar fissures in the sandstone specimens were cut using high-pressure water-jet cutting machine to produce an open fissure width of about 2.5 mm. In this research, different geometries of two non-coplanar fissures were produced by varying the ligament angle β while keeping the other three parameters constant ($\alpha = 30°$, $2a = 15$ mm, and $2b = 18$ mm) (Table 1). Note that, when the ligament angle β is equal to 30°, the two pre-existing fissures become coplanar, as reported in Yang (2011). All the tests were conducted at a strain rate of 8.125×10^{-6}.

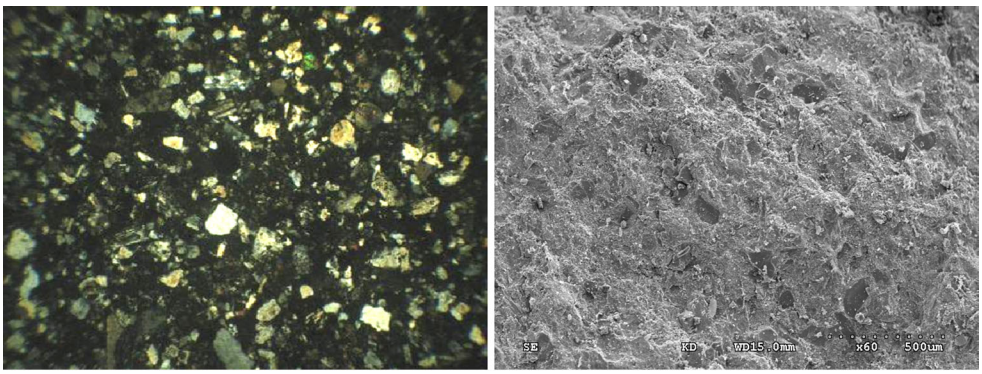

Fig. 1 Microscopic structure of the sandstone material in this research (Yang 2011). **a** Micropolariscope result (×40). **b** Scanning electron microscope (SEM) result (×60)

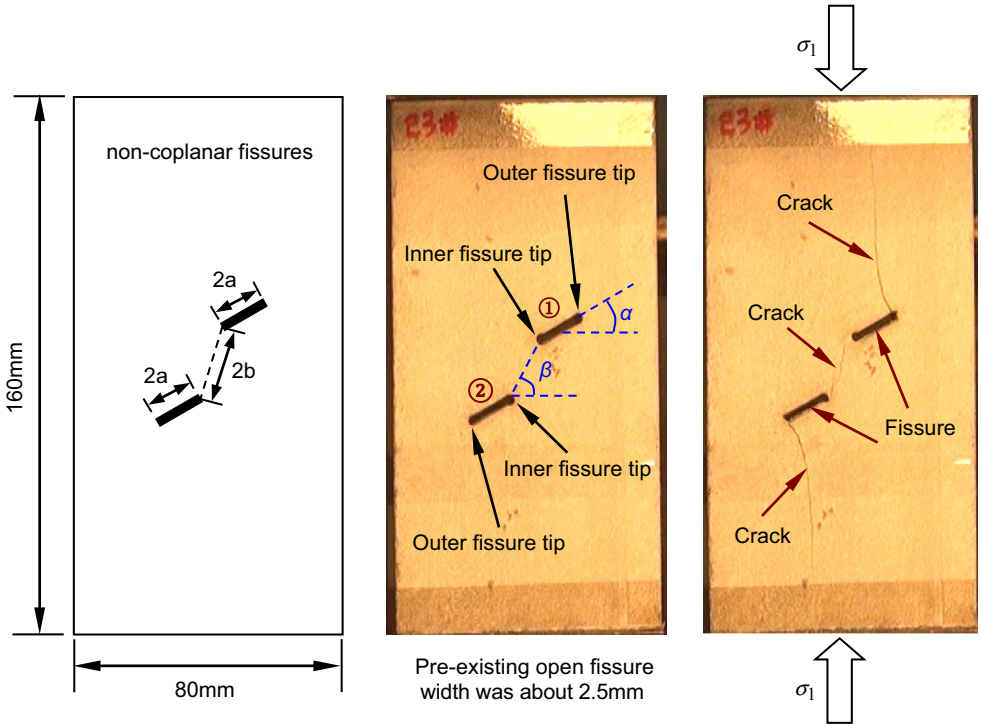

Fig. 2 Geometry of two non-coplanar fissures in a sandstone specimen, in which α is the fissure angle, β is the ligament angle, $2a$ is the fissure length, and $2b$ is the ligament length. In this research, two non-coplanar fissures in sandstone specimens were machined by high-pressure water-jet cutting

In this research, the crack evolution process of sandstone specimen containing two pre-existing fissures was snapped by a digital video camera. This is a continuous shooting progress, which yields 25 frames per second in order to ensure clear cracks.

3 Experimental Results

3.1 Strength and Deformation Behavior

Figure 3 shows the uniaxial stress–strain curve and crack coalescence process of an intact sandstone specimen under uniaxial compression (Yang 2011). From Fig. 3, it can be clearly seen that the tested sandstone is a kind of brittle rock which typically undergoes axial splitting tensile failure, and a loud failure sound could be heard during the dropping after peak strength. A more detailed analysis of the failure process of the intact specimen can be found in Yang (2011).

Figure 4 illustrates the axial stress–strain curves of brittle sandstone specimens containing two non-coplanar fissures with different ligament angles under uniaxial compression. For each ligament angle, we show two flawed specimens containing two non-coplanar fissures. From Fig. 4, it is clear that, for flawed specimens with the same ligament angle, the axial stress–strain curves exhibit similar behavior and show very good consistency. Based on

Table 1 Tested sandstone specimens containing two non-coplanar fissures under uniaxial compression

Specimen	*W*/mm	*H*/mm	*T*/mm	*α*/°	*β*/°	2*a*/mm	2*b*/mm	Note
A29#	80.9	157.6	31.0	N/A	N/A	N/A	N/A	Intact specimen
A16#	80.9	159.8	31.2	30	0	15	18	Flawed specimen
A22#	80.4	157.0	30.0	30	0	15	18	
A03#	80.9	159.2	31.7	30	30	15	18	
A11#	80.8	159.0	31.8	30	30	15	18	
A17#	80.3	159.2	29.6	30	60	15	18	
A23#	81.0	159.4	31.4	30	60	15	18	
A18#	81.0	157.6	31.4	30	90	15	18	
A24#	80.5	159.0	31.4	30	90	15	18	
A19#	80.3	159.4	29.2	30	120	15	18	

W width; *H* height; *T* thickness

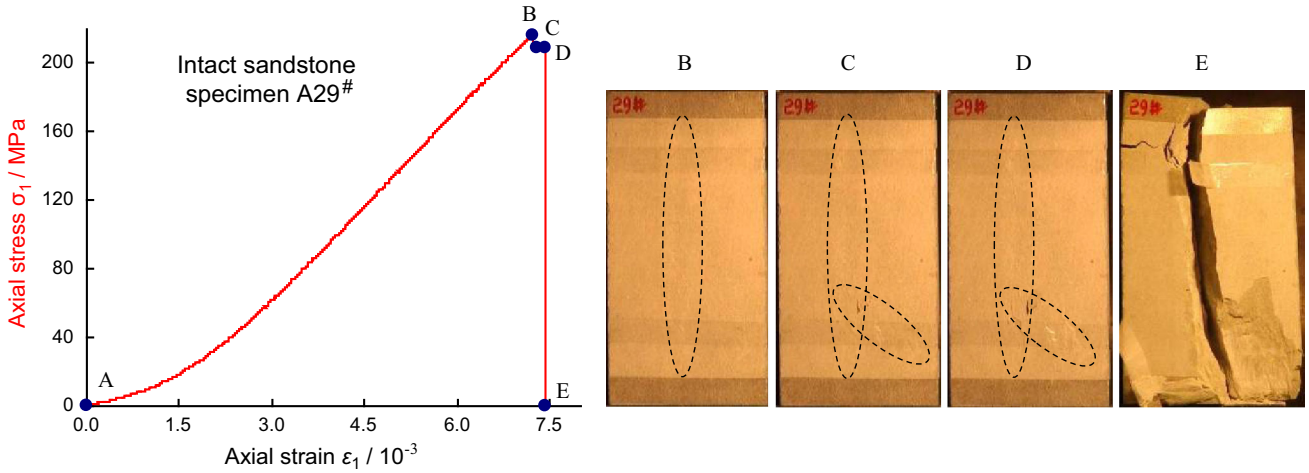

Fig. 3 Uniaxial stress–strain curve and crack coalescence process of an intact sandstone specimen under uniaxial compression (Yang 2011)

the above analysis, it can be concluded that heterogeneity has little effect on the deformation failure behavior of flawed specimens containing non-coplanar fissures with the same ligament angle β. Therefore, based on these experimental results, we investigated the effect of ligament angle on the mechanical parameters of brittle sandstone containing two non-coplanar fissures under uniaxial compression (see Fig. 5).

Figure 5 indicates that the ligament angle has a distinct effect on the strength and deformation behavior of sandstone specimens subjected to uniaxial compressive stress. Compared with the axial stress–strain curves of the intact specimen shown in Fig. 3, the stress–strain curves of sandstone specimens containing two non-coplanar fissures shown in Fig. 5 reveal several distinct stress drops, which result mainly from the initiation or coalescence of new cracks during loading.

Figure 6 presents the effect of ligament angle on the mechanical parameters of sandstone specimens containing two non-coplanar fissures under uniaxial compression. In Fig. 6, σ_c is the uniaxial compressive strength and E_S represents the elastic modulus, i.e., the slope of the approximately linear part of the stress–strain curve. The results show that the mechanical parameters of sandstone specimens containing two non-coplanar fissures are all lower than those of the intact specimen under uniaxial compression. It should be noted that, in the following analysis, the mechanical parameters are all the average values of two specimens for the same ligament angle, except for $\beta = 120°$.

In accordance with Fig. 6a, it can be seen that the uniaxial compressive strength of specimens containing two non-coplanar fissures ranges from 79.46 MPa ($\beta = 60°$) to 144 MPa ($\beta = 120°$). As the ligament angle β increases from 0° to 30°, the uniaxial compressive strength of flawed specimens increases from 99.39 MPa to 103.6 MPa, which indicates that the σ_c of specimens containing two non-coplanar fissures is not directly dependent on the ligament angle for β smaller than 30°. However, the σ_c of flawed specimens decreases from 103.6 MPa to 79.46 MPa when

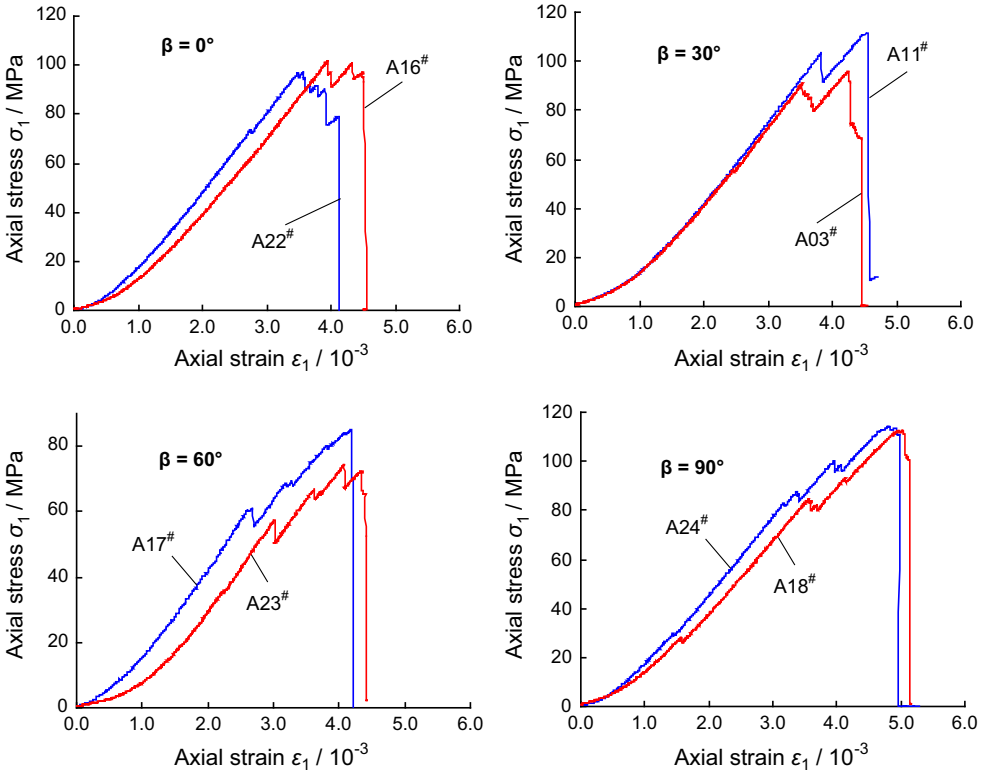

Fig. 4 Effect of heterogeneity on axial stress–strain curves of sandstone specimens containing two non-coplanar fissures ($2a = 15$ mm and $2b = 18$ mm) under uniaxial compression

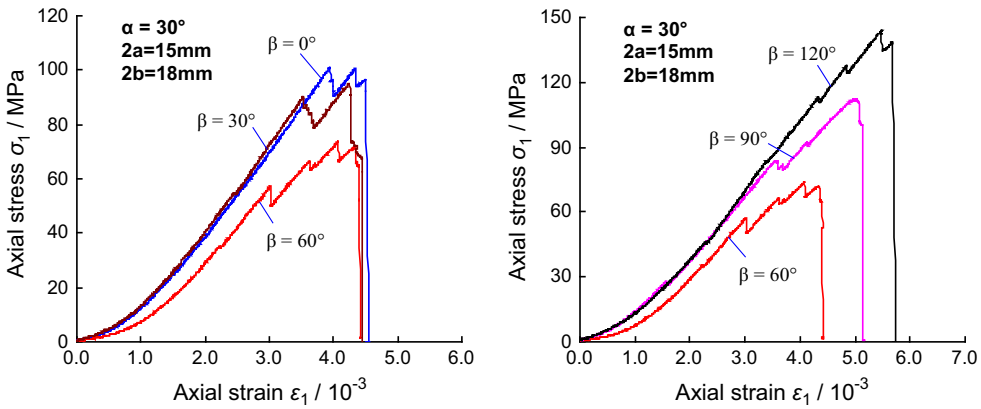

Fig. 5 Axial stress–strain curves of sandstone specimens containing two non-coplanar fissures under uniaxial compression

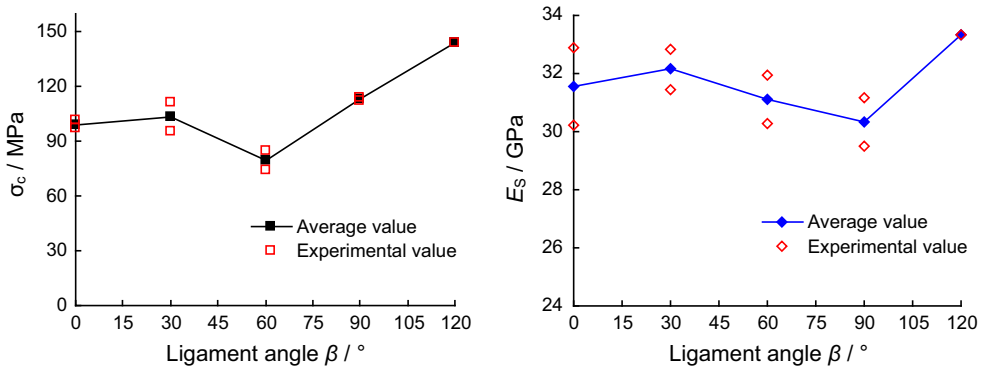

Fig. 6 Effect of ligament angle on the peak strength and elastic modulus of sandstone specimens containing two non-coplanar fissures under uniaxial compression ($\alpha = 30°$, $2a = 15$ mm, and $2b = 18$ mm)

β increases from 30° to 60°. Then, the σ_c of flawed specimens increases from 79.46 MPa to 144 MPa as β increases from 60° to 120°, which reveals that the effect of the ligament angle on the uniaxial compressive strength of specimens containing two non-coplanar fissures is very obvious for β greater than 30°.

The elastic modulus of the intact specimen was 37.41GPa (Yang 2011). However, the elastic modulus of specimens containing two non-coplanar fissures ranged from 30.33GPa ($\beta = 90°$) to 33.35GPa ($\beta = 120°$), while the reduction of elastic modulus was between 10.9 and 18.9 %. In general, the elastic modulus of sandstone is not dependent distinctly on the ligament angle. The average elastic modulus of all the specimens containing two coplanar fissures was about 31.52GPa, which reaches 84.3 % of the elastic modulus, ~37.41GPa of the intact specimen, and the dispersion coefficient (the percentage of the differential value between the maximum and minimum value to the average value) is approximately 12.2 %.

3.2 Fracture Coalescence Behavior of Specimen for β Smaller than or Equal to 60°

The ultimate failure modes of sandstone specimens containing two non-coplanar fissures under uniaxial compression are presented in Fig. 7, and the results differ markedly from that of the intact specimen shown in Fig. 3. From Fig. 7, it can be seen that the ultimate failure modes of sandstone specimens subject to uniaxial compressive stress are obviously dependent on the ligament angle. It should also be noted that the ultimate failure mode of each sandstone specimen is a mixture of several crack coalescences (Yang 2011). Therefore, in the present and next sections, we investigate crack initiation and coalescence in sandstone specimens containing two non-coplanar fissures using photographic monitoring.

Figure 8 presents the crack initiation and coalescence process of sandstone specimens containing two non-coplanar fissures for $\beta = 0°$. The figure shows that tensile wing crack 1 was initiated at the outer tip of fissure ② and coalesced towards the end surface of the specimen along the direction of axial stress. When the specimen was loaded until the peak point *b*, tensile crack 2^a was initiated at the inner tip of fissure ②, and tensile cracks 2^b and 2^c from the inner and outer tips of fissure ①, respectively. In the process of initiating tensile cracks 2^a–2^c, the axial stress dropped from the peak strength ~101.44 to 95.8 MPa.

Afterwards, with the increase of axial deformation, the specimen was loaded to point *c*, and tensile crack 3^a was initiated at the outer tip of fissure ②, whereas anti-tensile crack 3^b was observed from the outer tip of fissure ①, the above coalescence process resulting in an obvious stress drop from 96.5 to 90.61 MPa. Notice that, after this drop, due to minor damage to the supporting structure in the specimen at point *c*, the axial stress increased with the axial deformation at an average modulus of approximately 30.91GPa, which was a little lower than the elastic modulus ~32.23GPa before peak strength.

When the specimen was loaded to point *e*, a far-field crack 4 was observed in the upper central region of the specimen, which also caused the axial stress to drop from 100.5 to 94.08 MPa in an almost constant axial strain. With the increase of axial deformation, the axial stress then began to increase slowly, while the average modulus of the specimen was much lower, only ~19.4GPa, possibly due to more damage in the specimen at point *e*. When the specimen reached point *f*, anti-tensile crack 5^a was initiated at the inner tip of fissure ① and coalesced with crack 4, but

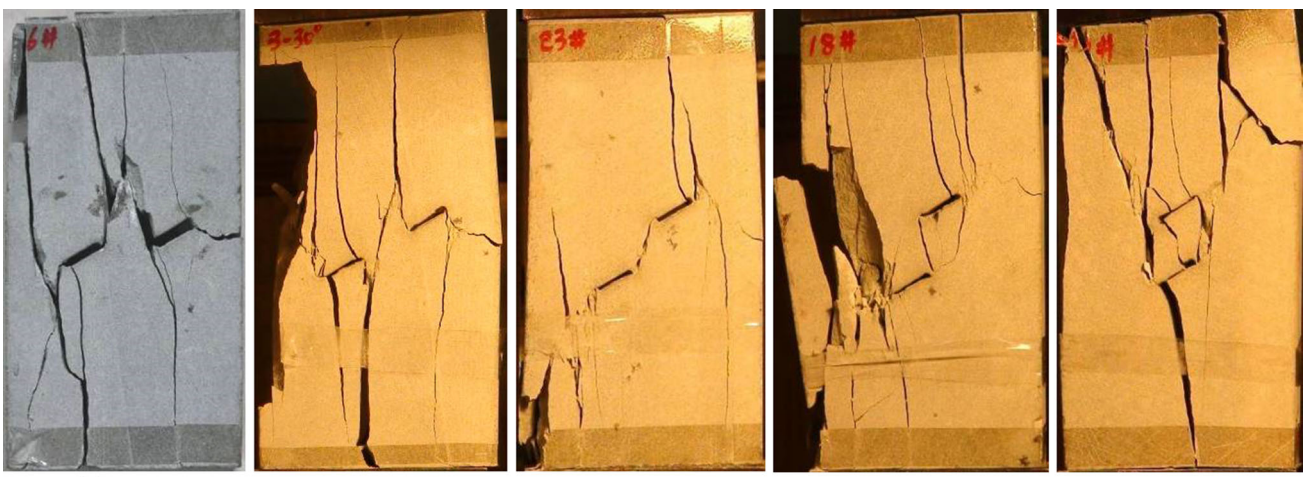

(a) β = 0° **(b)** β = 30° **(c)** β = 60° **(d)** β = 90° **(e)** β = 120°

Fig. 7 Ultimate failure modes of sandstone specimens containing two non-coplanar fissures under uniaxial compression

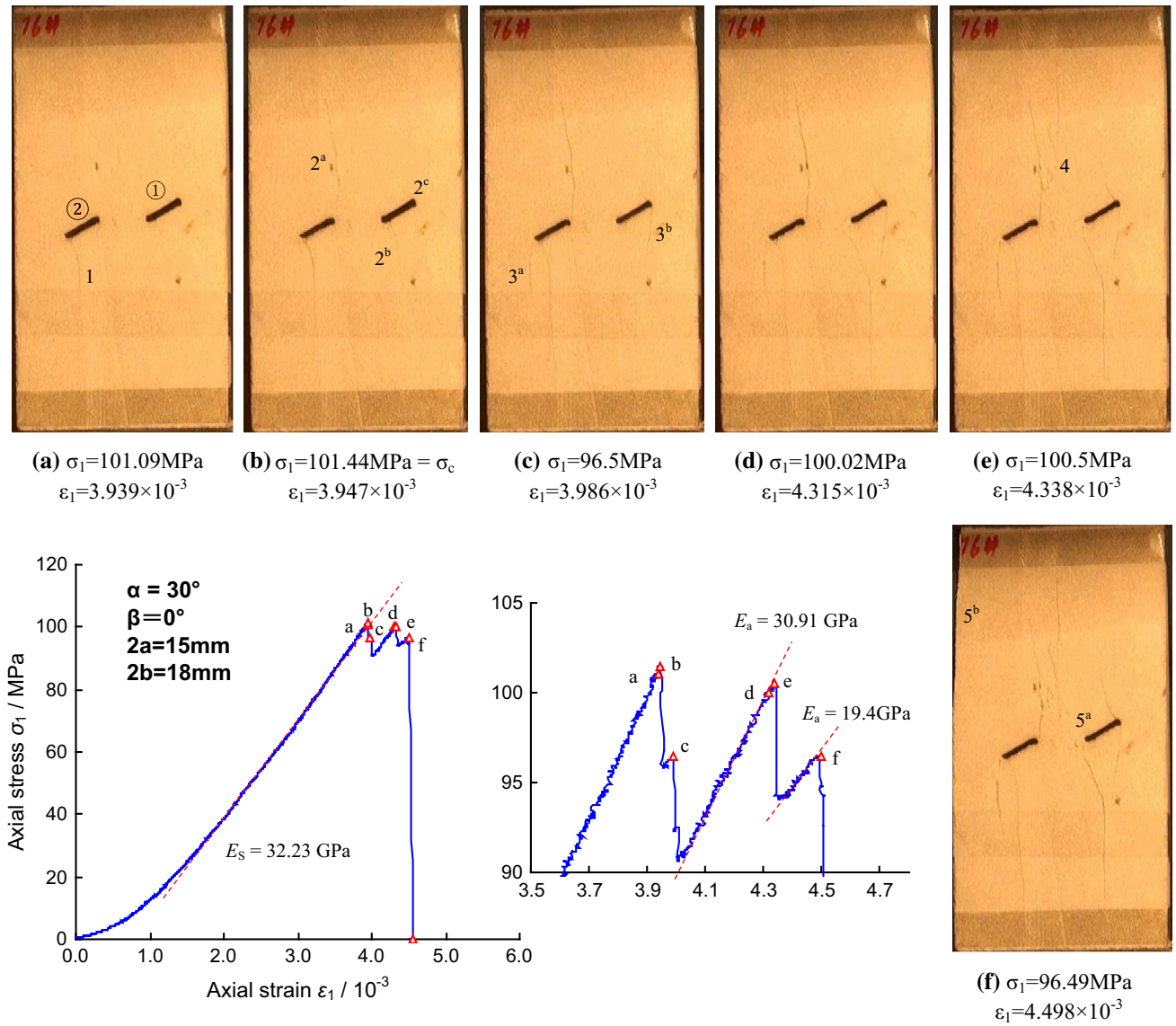

Fig. 8 Crack initiation and coalescence process of sandstone specimens containing two non-coplanar fissures for $\beta = 0°$

the far-field crack 5^b was observed in the left top region of the specimen. After point *f*, the specimen incurred ultimately unstable failure and the axial stress dropped rapidly to zero in three seconds.

Compared with the fracture coalescence process of the specimen with $\beta = 0°$ shown in Fig. 8, the crack initiation and coalescence processes of sandstone specimens containing two non-coplanar fissures for $\beta = 60°$ are distinctly different, as shown in Fig. 9. As the figure shows, the fracture coalescence process of the specimen has a good correspondence with the axial stress–strain curves. When the specimen was loaded to points *a* (about 48 % σ_c) and *b* (about 69.8 % σ_c), four cracks were initiated from the tips of pre-existing fissures. Note that the cracks 2^a–2^b did not coalesce due to interaction of the stress fields between the inner tips of two non-coplanar fissures. The wing tensile cracks 1^a and 1^b were initiated from the outer tips of fissure ① and ②, respectively, and coalesced along the direction of axial stress. At point *a*–*b*, the fracture coalescence of the specimen did not lead to a distinct stress drop, but had an obvious turning characteristic. When being loaded to point *c*, shear crack 2 formed rapidly between the inner tips of fissure ① and ②, and, simultaneously, the length and width of tensile cracks 1^a and 1^b all increased, which induced a distinct stress drop from 57.39 to 50.16 MPa.

With the increase of axial deformation, the axial stress began to increase slowly at an average modulus of approximately 28.41 GPa, which was a little lower than the elastic modulus ~30.46 GPa. After reaching point *e* (about 90 % σ_c), tensile crack 3 was initiated from the outer tip of fissure ② and coalesced along the direction of axial stress

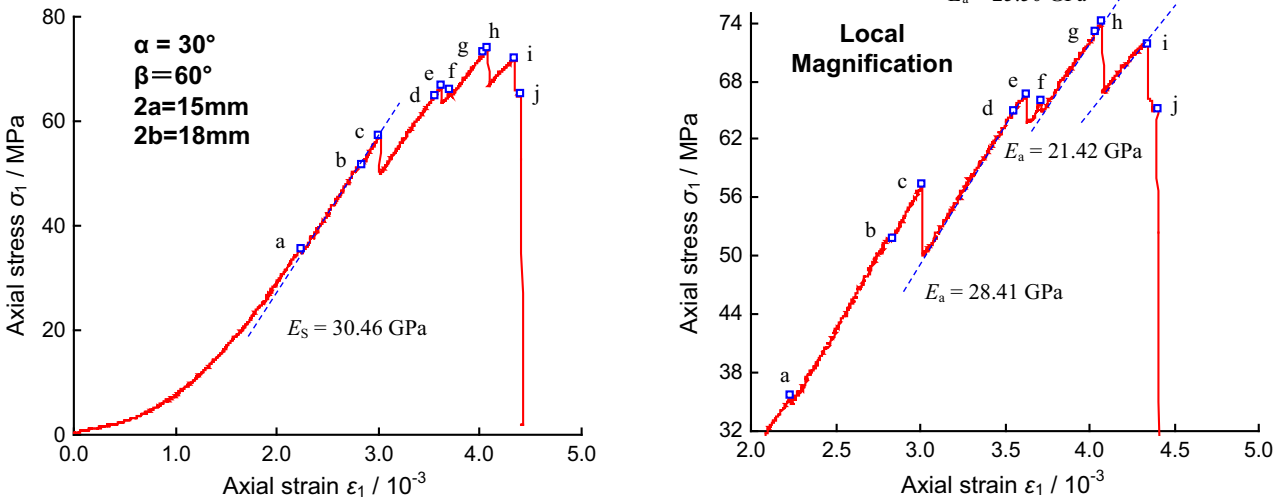

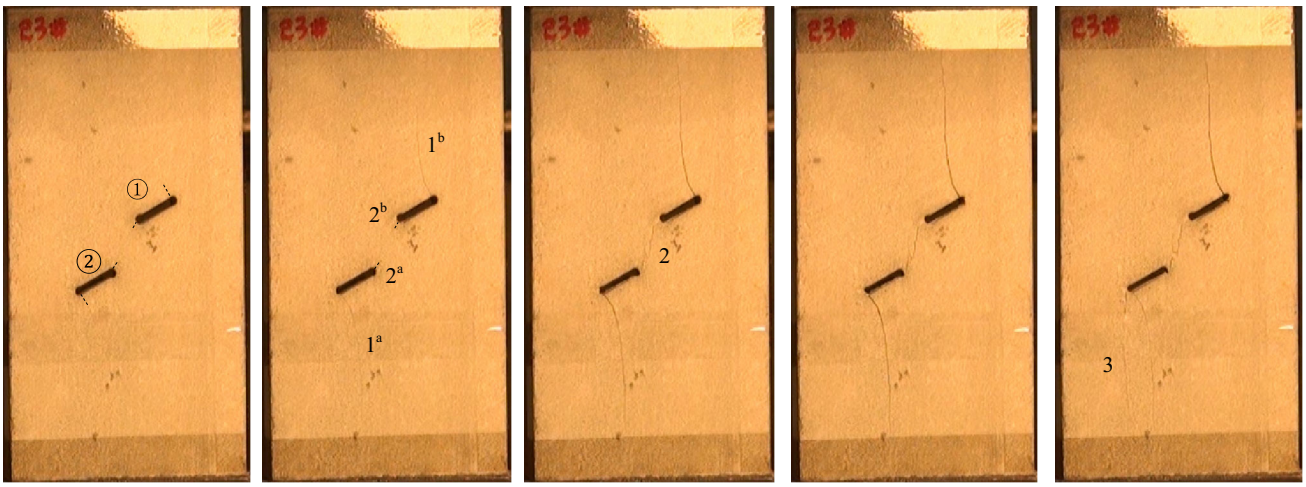

(a) σ_1=35.6 MPa ε_1=2.234×10^{-3} **(b)** σ_1=51.71 MPa ε_1=2.834×10^{-3} **(c)** σ_1=57.39 MPa ε_1=3.008×10^{-3} **(d)** σ_1=64.94 MPa ε_1=3.560×10^{-3} **(e)** σ_1=66.69 MPa ε_1=3.626×10^{-3}

(f) σ_1=66 MPa ε_1=3.713×10^{-3} **(g)** σ_1=73.14MPa ε_1=4.036×10^{-3} **(h)** σ_1=74.11 MPa = σ_c ε_1=4.072×10^{-3} **(i)** σ_1=71.88 MPa ε_1=4.343×10^{-3} **(j)** σ_1=65.05MPa ε_1=4.404×10^{-3}

Fig. 9 Crack initiation and coalescence process of sandstone specimens containing two non-coplanar fissures for $\beta = 60°$

towards the bottom edge of the specimen. For this process, a stress drop from 66.69 to 63.5 MPa could be seen in the axial stress–strain curve of the specimen. When the specimen was loaded to point *f*, tensile crack 4 was initiated from the outer tip of fissure ①, but did not coalesce to the top edge of the specimen along the direction of axial stress. For the moment, the specimen had a minor stress drop from 66 to 64.84 MPa. Afterwards, the axial stress increased slowly with the increasing deformation at an average modulus of 25.50 GPa, which is lower than the previous average modulus of 28.41 GPa due to some failures of the supporting structure in the specimen at point *f*.

The continuous increase of axial deformation led to the specimen being loaded to the peak point *h* (100 % σ_c), and cracks 5^a and 5^b formed simultaneously. However, it should be noticed that crack 5^a did not initiate from the outer tip of fissure ① and crack 5^b initiated in the right region of the specimen along the direction of axial stress. The fracture of crack 5 led to an obvious stress drop from 74.11 to 66.85 MPa. After this stress drop, the axial stress increased with the axial deformation at a lower average modulus of 21.42 GPa. When the specimen was loaded to point *i*, crack 5^b coalesced and merged with crack 5^a. After point *i*, the axial stress continued to drop and, when it dropped to point *j*, tensile crack 6 was initiated from the outer tip of fissure ②. The specimen rapidly underwent unstable failure and some splitting failures were observed during the ultimate dropping.

3.3 Fracture Coalescence Behavior of Specimen for β Greater than 60°

Figure 10 illustrates the crack initiation and coalescence processes of sandstone specimens containing two non-coplanar fissures for $\beta = 90°$. From Fig. 10, it can be seen that, before point *a* ($\sigma_1 = 27.77$ MPa = 24.8 % σ_c), the stress concentration at the inner and outer tips of two fissures did not reach the material strength close to the tips, and, consequently, did not result in a crack initiation. However, when the axial stress was loaded up to point *a*, tensile wing cracks (cracks 1^a–1^d) were initiated simultaneously from the inner and outer tips of fissure ① and ②. It should be noted that the first crack was initiated at the angle of about 90° with fissures ① and ②, and then gradually departed towards the direction of axial stress. However, in the deformation process from point *a* to *d* ($\sigma_1 = 81.39$ MPa = 72.6 % σ_c), with an increase in the axial deformation, although the axial stress increased continuously, no new cracks were observed in the specimen. It should be noted that tensile cracks 1^a and 1^b propagated towards the edge of the specimen along the direction of axial stress, but tensile cracks 1^c and 1^d only propagated a little due to the interaction of stress fields between two pre-existing fissures. Moreover, the widths of four tensile cracks (cracks 1^a–1^d) all increased.

The continuous increase of axial deformation led to the specimen being loaded to point *e* ($\sigma_1 = 84.04$ MPa = 75.0 % σ_c), and, at this moment, crack 2 emanated from the outer tip of fissure ② and propagated in the upward direction of the specimen, which also led to a minor stress drop in the axial stress–strain curve. When the axial stress was loaded up to point *f*, coalescence occurred in the ligament region between the two fissures, and tensile crack 3^b emanated rapidly between the inner tips of fissures ① and ②. At the same time, crack 3^a was also observed from the outer tip of fissure ① and propagated in the downward direction of the specimen, which also led to a minor stress drop from 83.72 to 79.71 MPa. Note, in the deformation process from point *e* to *f*, two previously open tensile cracks, 1^c and 1^d, closed due to the coalescence of crack 3^b in the specimen. Afterwards, when the specimen was loaded to point *g*, tensile crack 4 was initiated from the outer tip of fissure ② and propagated in the downward direction towards the bottom edge of the specimen, which also led to a minor stress drop in the axial stress–strain curve. After point, with the increase of deformation, the specimen was loaded to point *h*, and tensile crack 5 emanated from the outer tip of fissure ① and propagated along the direction of major principal stress towards the top edge of the specimen.

When the specimen was loaded to the peak strength (i.e., point *i*), the corresponding axial stress and axial strain were 112.06 MPa and 5.004×10^{-3}, respectively. At this moment, no new cracks were observed in the specimen, but the widths of some cracks (e.g., cracks 4–5) increased. After the peak strength, as further increase of axial deformation occurred, the specimen could not reach a higher axial stress due to serious damage to the supporting structure. When the axial stress of the specimen dropped to point *j*, tensile crack 6^a emanated from the outer tip of fissure ②, and the other tensile crack (6^b) was initiated in the left region of the specimen, which did not emanate from the tips of fissures. The specimen then underwent unstable failure and some spalling failures were observed during the ultimate drop, as shown in Fig. 7d. At the same time, some axial tensile cracks and lateral cracks were also observed, which did not emanate from the tips of fissures.

Compared with those for β smaller than or equal to 90°, the crack initiation and coalescence processes of sandstone specimens containing two non-coplanar fissures for $\beta = 120°$ clearly differed, which could be seen from Fig. 11. When the axial stress was loaded to point *a* ($\sigma_1 = 46.30$ MPa = 32.2 % σ_c), three tensile cracks (1^a–1^c) were observed. Tensile wing cracks 1^a and 1^b were from the outer tip of fissures ① and ②, respectively.

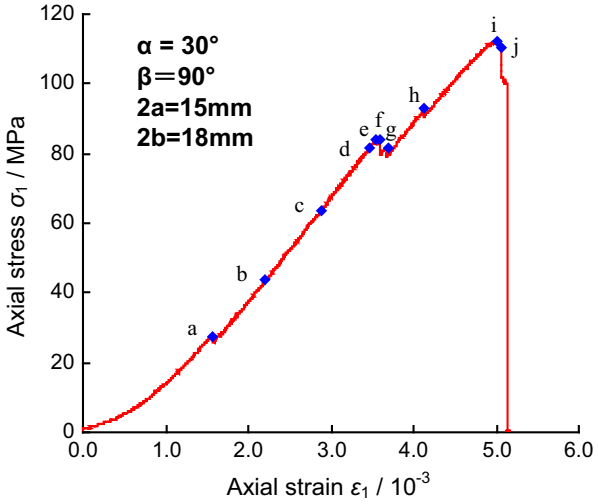

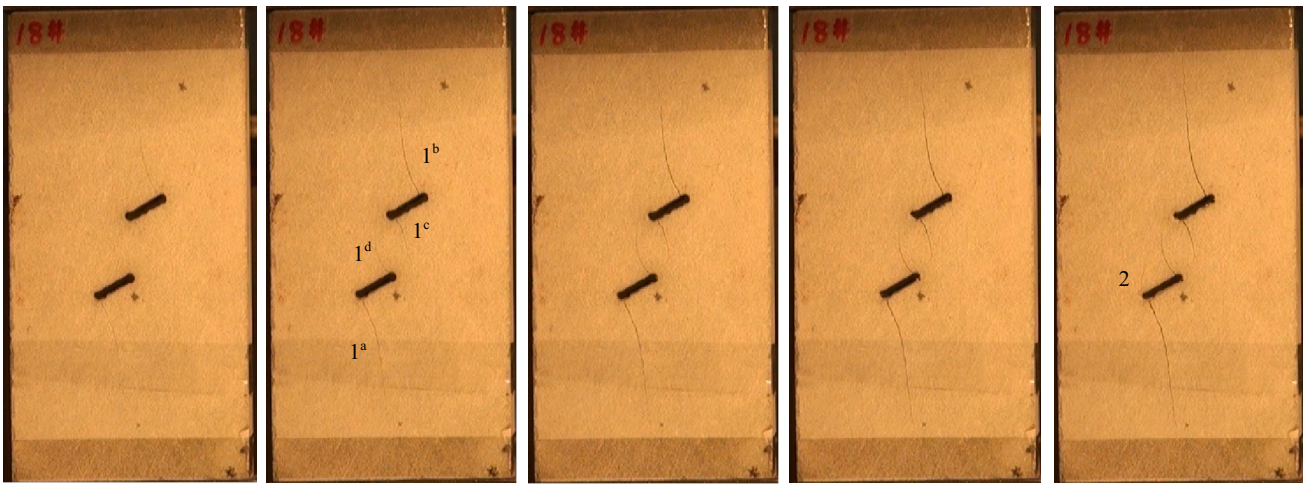

(a) σ_1=27.77 MPa ε_1=1.564×10^{-3} **(b)** σ_1=43.77 MPa ε_1=2.211×10^{-3} **(c)** σ_1=63.85 MPa ε_1=2.881×10^{-3} **(d)** σ_1=81.39 MPa ε_1=3.465×10^{-3} **(e)** σ_1=84.04 MPa ε_1=3.550×10^{-3}

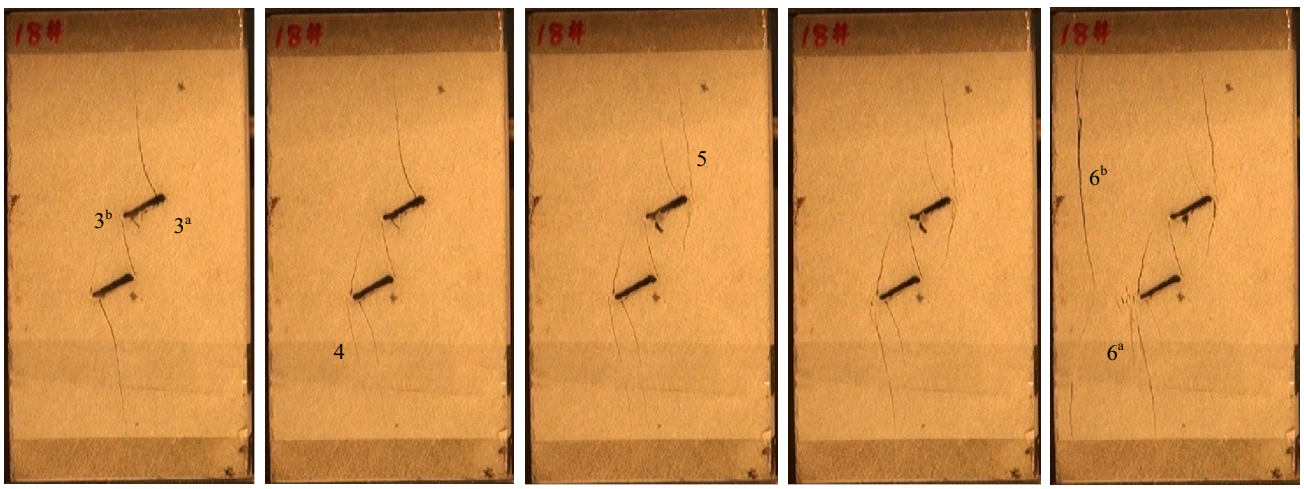

(f) σ_1=83.72 MPa ε_1=3.603×10^{-3} **(g)** σ_1=81.88 MPa ε_1=3.688×10^{-3} **(h)** σ_1=92.75 MPa ε_1=4.116×10^{-3} **(i)** σ_1=112.06 MPa = σ_c ε_1=5.004×10^{-3} **(j)** σ_1=110.4 MPa ε_1=5.060×10^{-3}

Fig. 10 Crack initiation and coalescence process of sandstone specimens containing two non-coplanar fissures for $\beta = 90°$

At this moment, tensile crack 1^c coalesced between the inner tip of fissure ① and a certain distance away from the inner tip of fissure ②, and the coalescence path of crack 1^c was very circuitous. When the specimen was loaded to point b ($\sigma_1 = 73.42$ MPa $= 51.0\ \%\ \sigma_c$) from point a, although no new cracks were observed, the widths of three tensile cracks (1^a–1^c) increased greatly, and tensile wing cracks 1^a and 1^b propagated towards the boundary of the specimen. The two anti-tensile wing cracks 2 and 3 were then initiated from the outer tip of fissures ② and ①, respectively. They propagated towards the inner fissure tip of the specimen along the direction of axial stress. When the specimen was loaded to point e ($\sigma_1 = 104.48$ MPa $= 72.6\ \%\ \sigma_c$), anti-tensile wing crack 2 coalesced between the outer tip of fissure ② and the inner tip of fissure ①, whereas anti-tensile wing crack 3 coalesced between the outer tip of fissure ① and the inner tip of fissure ②. The continuous increase of axial deformation led to the specimen being loaded to point f ($\sigma_1 = 113.32$ MPa $= 78.7\ \%\ \sigma_c$), and, at this moment, far-field crack 4 emanated from a position near crack 3 and propagated in the downward direction towards the bottom boundary of the specimen, which also led to a minor stress drop in the axial stress–strain curve.

After far-field crack 4 was initiated, with the increase of axial deformation, the specimen was loaded to point g ($\sigma_1 = 126.59$ MPa $= 87.9\ \%\ \sigma_c$), and far-field crack 5 emanated from a position near crack 2 and propagated in the upward direction towards the top boundary of the specimen, which also led to a minor stress drop in the axial stress–strain curve. With the continuous increase of axial deformation, when the specimen was loaded to point i ($\sigma_1 = 143.72$ MPa $= 99.8\ \%\ \sigma_c$), far-field crack 6 was observed in the right top region of the specimen, which propagated along the direction of axial stress. When the specimen was loaded to the peak point j, crack 6 linked with crack 4, and a new tensile crack 7 was observed in the left region of the specimen and propagated along the direction of axial stress. However, after the peak strength, the specimen underwent unstable failure and fewer spalling failures were observed during the ultimate drop, as shown in Fig. 7e. At the same time, some axial tensile cracks and lateral cracks were also observed, which did not emanate from the tips of fissures.

4 Numerical Modeling and Simulated Results

4.1 Numerical Model and Micro-Parameters

In this section, the numerical model and micro-parameters for the brittle sandstone specimens will be investigated. A particle flow code (PFC^{2D}) was chosen to simulate crack evolution behavior of brittle sandstone containing two non-coplanar fissures (Fig. 12). Although PFC^{2D} is only two-dimensional, it can be used to simulate many scientific problems in rock mechanics and rock engineering, including laboratory experiments on the failure mechanical behavior of rock material (Debecker and Vervoort 2013; Jia et al. 2013; Zhang and Wong 2013), crack initiation, propagation, and coalescence in rock specimens containing pre-existing fissures (Yang and Huang 2014; Zhang and Wong 2012), split Hopkinson pressure bar (SHPB) dynamic test problems (Li et al. 2014), large-scale slope failure (Behbahani et al. 2013), etc. In PFC^{2D}, there are two kinds of micro-bond models (Cho et al. 2007): one is a contact bond model (CBM) and the other is a parallel bond model (PBM). In this research, we chose the PBM for the numerical simulation, because the PBM is more realistic for rock material modeling, in which the bonds may break in either tension or shearing with an associated reduction in stiffness (Cho et al. 2007).

In using PFC^{2D}, one intact numerical specimen was first generated, and the scale of the numerical specimen is similar to that of the experimental specimen, i.e., 80 mm wide and 160 mm high. All specimens had a height-to-width ratio of 2.0 to ensure a uniform stress state within the central part of the specimens. Each numerical intact specimen was discretized into 25,552 particles with 51,064 contacts and 66,431 parallel bonds. The particle size followed a uniform distribution ranging from 0.3 to 0.48 mm. The average unit weight of the sandstone specimen was about 2650 kg/m^3. The numerical simulations for sandstone specimens were carried out on a three-dimensional model with one unit thickness. It should be noted that, in PFC^{2D}, the numerical model is neither in 2-D plane stress state nor in 2-D plane strain state. An external displacement is applied to the top of the rock specimens at a constant rate of 0.05 m/s in the axial direction.

In this research, the choice of the loading rate for the numerical simulation can be explained as follows (Yang et al. 2014). In the past studies, Zhang and Wong (2013) had analyzed in detail the influence of loading rate on the cracking behavior of specimens containing a single fissure and two parallel fissures under uniaxial compression by PFC^{2D}, which showed that the crack initiation stress and uniaxial compressive strength remained basically constant when the loading rate was increased from 0.005 to 0.08 m/s, even for different flaw inclination angles. Therefore, we used the loading rate of 0.05 m/s to carry out the numerical simulation, which was also the same as that by Potyondy and Cundall (2004) for uniaxial compression, biaxial compression, and Brazilian numerical simulation. In the simulation, the PFC^{2D} will compute the critical time step first and assign a reasonable time step before each cycle.

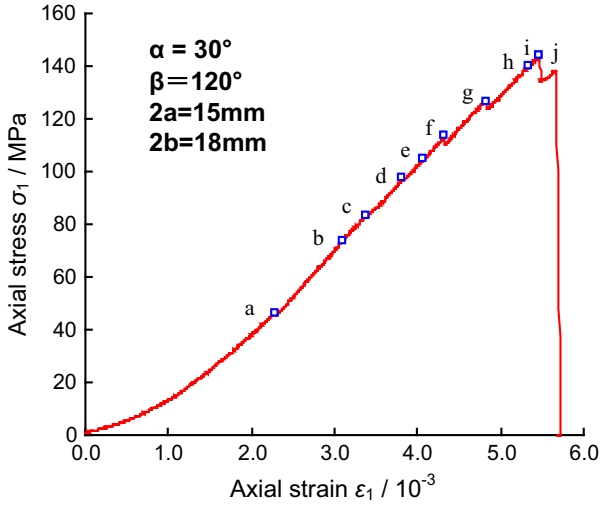

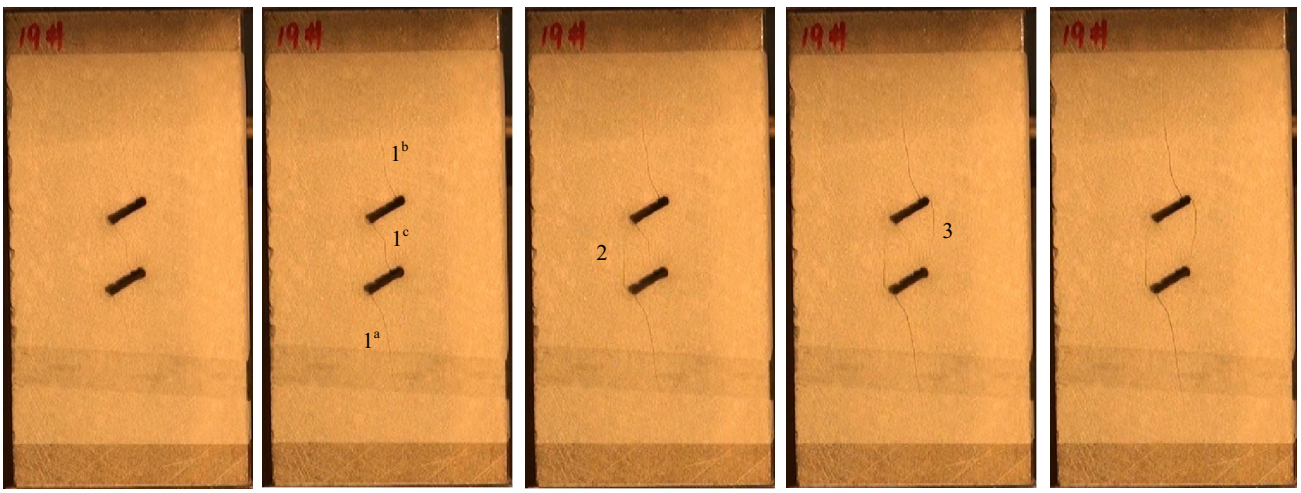

(a) σ_1=46.30 MPa ε_1=2.29×10^{-3} **(b)** σ_1=73.42 MPa ε_1=3.094×10^{-3} **(c)** σ_1=83.44 MPa ε_1=3.389×10^{-3} **(d)** σ_1=97.52 MPa ε_1=3.825×10^{-3} **(e)** σ_1=104.48 MPa ε_1=4.064×10^{-3}

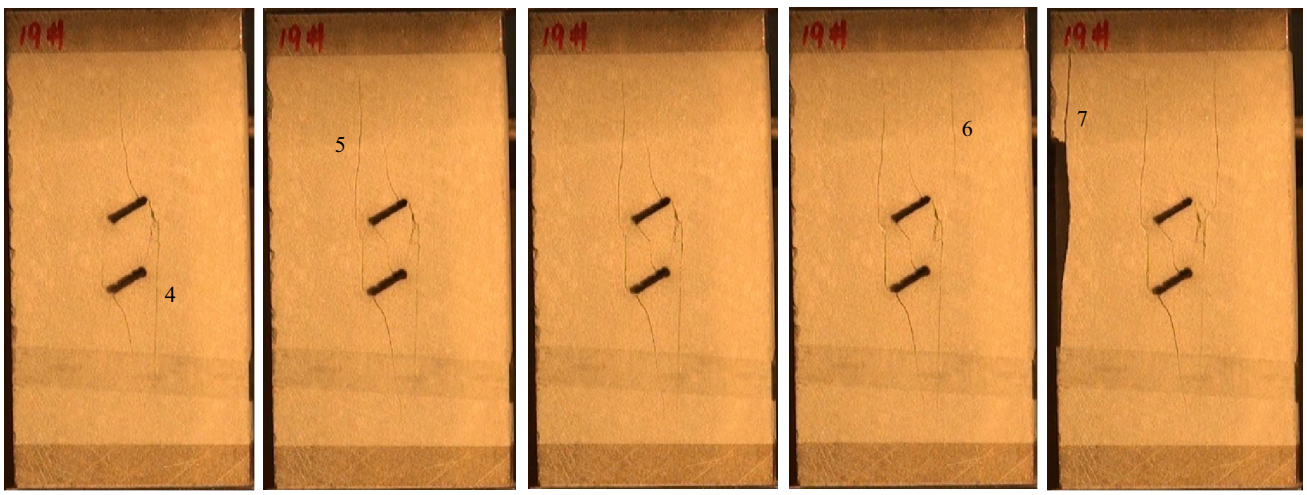

(f) σ_1=113.32 MPa ε_1=4.332×10^{-3} **(g)** σ_1=126.59 MPa ε_1=4.836×10^{-3} **(h)** σ_1=139.64 MPa ε_1=5.338×10^{-3} **(i)** σ_1=143.72 MPa ε_1=5.459×10^{-3} **(j)** σ_1=144 MPa = σ_c ε_1=5.473×10^{-3}

Fig. 11 Crack initiation and coalescence process of sandstone specimens containing two non-coplanar fissures for $\beta = 120°$

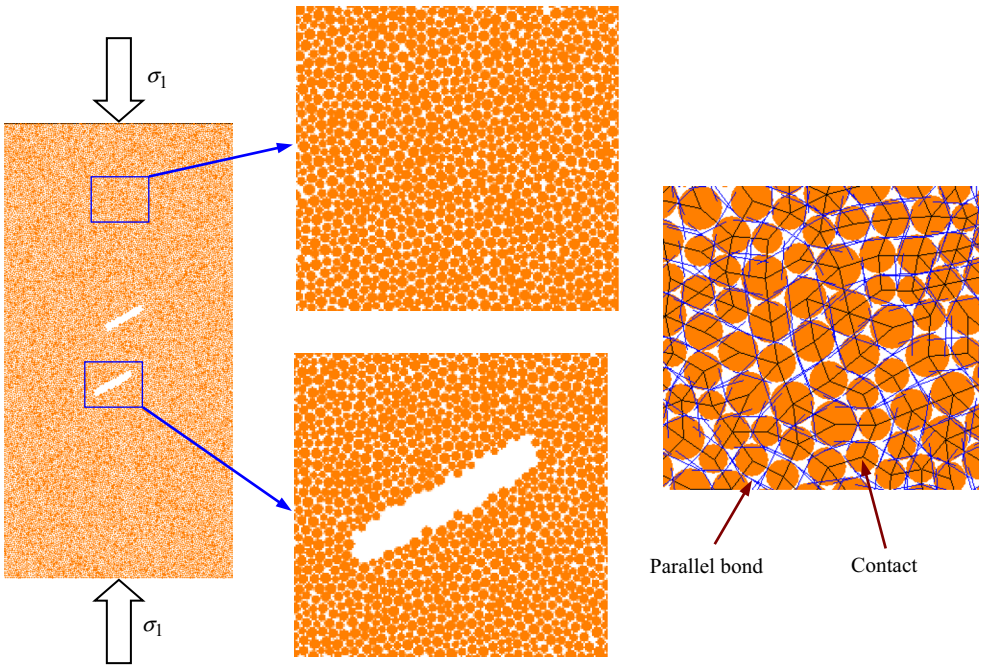

Fig. 12 Numerical model of sandstone specimen containing two non-coplanar fissures (by PFC^{2D})

For example, if the time step is equal to 1×10^{-8} s/step, 0.05 m/s can be translated to 5×10^{-7} mm/step, which means that it requires 2,000,000 steps to move the specimen for 1 mm. Thus, this loading rate of 0.05 m/s is low enough in the PFC simulation.

As is well known, it is very difficult to determine micro-parameters in PFC^{2D} experimentally. However, in order to validate the particle properties used in the numerical modeling, it is essential to establish a correlation between the macro-behavior (i.e., the axial stress–strain curve, triaxial peak strength and elastic modulus, the ultimate failure mode, and the crack coalescence process) and the micro-parameters. During the calibration process, the micro-parameters were confirmed using trial and error. The macroscopic behavior of intact rock-like specimen under uniaxial compression obtained by experimentation was used in this research to calibrate the micro-parameters. The macroscopic results obtained by numerical simulation after each trial were used to check the micro-parameters. This process was repeated until the numerical results achieved good agreement with the experimental results.

Table 2 lists the micro-parameters used in the PFC^{2D} model for rock-like specimens in this research. The Young's moduli of the particle and the parallel bond are both 26 GPa, and the ratios of normal to shear stiffness of the particle and the parallel bond are both 1.3. The particle friction coefficient is 0.35. The mean value of the parallel-bond normal strength (σ_n) and the mean value of the parallel-bond shear strength (τ_n) are, respectively, 145 MPa and 215.08 MPa, and the ratio of σ_n/τ_n is about 0.67.

4.2 Numerically Simulated Stress–Strain Curves

Figure 13 illustrates the comparison of the experimental and numerical results of an intact sandstone specimen under uniaxial compression. From Fig. 13, it can be seen that the numerically simulated curve under uniaxial compression agrees well with the experimental curve, except for the initial phase of the curve. The experimental stress–strain curve of the intact sandstone specimen at low stress levels shows downward concave and initial non-linear deformation, which mainly results from the closure of some primary cracks, pores, and voids in the tested sandstone specimen. The uniaxial compressive strength and elastic modulus of the intact sandstone specimen obtained by numerical simulation are, respectively, 212.82 MPa and 38.94 GPa, which are approximately equal to those obtained by experiment (i.e., 215.98 MPa for uniaxial compressive strength and 37.41 GPa for elastic modulus). However, the peak strain of the intact specimen obtained by numerical simulation (5.619×10^{-3}) is obviously lower than that obtained by experiment (i.e., 7.240×10^{-3}), as a result of an obvious stage of initial non-linear deformation during the experiment. The numerical specimen also undergoes typically axial splitting tensile failure, which approximates the experimental failure mode. In general, the numerical simulation method can replicate the complete process of deformation and failure of brittle sandstone specimens, especially the localization of deformation and failure (Xu et al. 2006).

A typical comparison of experimental and numerical stress–strain curves of sandstone specimens containing two

Table 2 The micro-parameters used in the PFC^{2D} model for sandstone specimens in this research

Micro-parameters	Values	Remarks
Young's modulus of the particle, E_c (GPa)	26	
Young's modulus of the parallel bond, $\bar{E}_c$(GPa)	26	
Ratio of normal to shear stiffness of the particle, k_n/k_s	1.3	
Ratio of normal to shear stiffness of the parallel bond, $\bar{k}_n/\bar{k}_s$	1.3	
Particle friction coefficient (μ)	0.35	
Parallel-bond normal strength (σ_n), mean (MPa)	145	Normal distribution
Parallel-bond normal strength, standard deviation (MPa)	18.08	
Parallel-bond shear strength (τ_n), mean (MPa)	215.08	Normal distribution
Parallel-bond shear strength, standard deviation (MPa)	29.93	

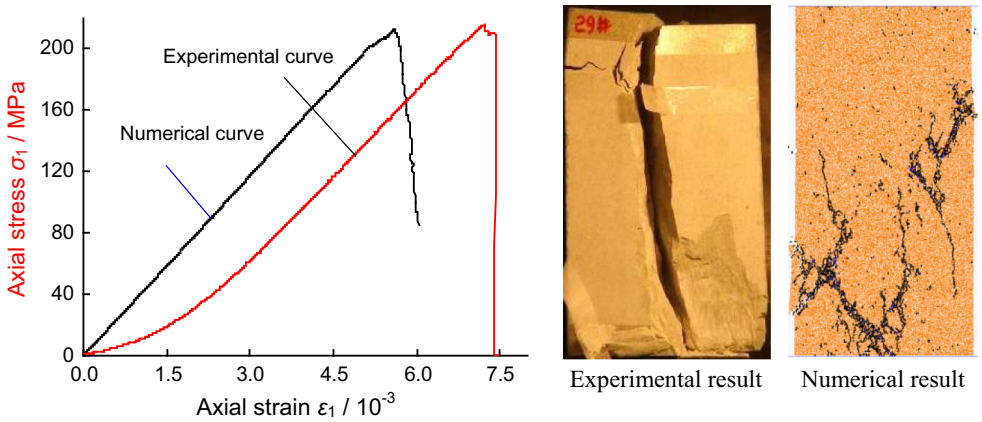

Fig. 13 Comparison of experimental and numerical results for intact sandstone specimen under uniaxial compression

non-coplanar fissures (for $\beta = 60°$ and 90°) under uniaxial compression is illustrated in Fig. 14. In Fig. 14, it can be seen that the numerically simulated deformation processes of the specimens containing two non-coplanar fissures are in good agreement with the experimental stress–strain curves.

Figure 15 shows the comparison of experimental and numerical mechanical parameters for brittle sandstone specimens containing two non-coplanar fissures under uniaxial compression. From Fig. 15a, it is clear that the uniaxial compressive strength of brittle sandstone specimens containing two non-coplanar fissures simulated by PFC^{2D} shows a similar trend with the increase of ligament angle β. However, the simulated uniaxial compressive strength is higher than that obtained by experiment for the same β. Furthermore from Fig. 15b, we can also conclude that the numerical elastic modulus of brittle sandstone specimens containing two non-coplanar fissures is higher by 3 GPa than that obtained by experiment for the same β. The above descriptions can be explained as follows. On one hand, it is due to the fact that the numerical simulation was 2-D analysis by materials composed of

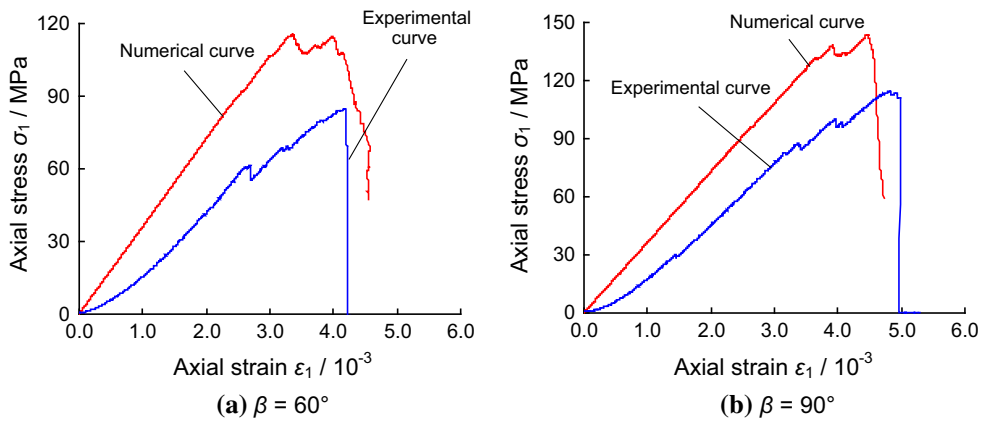

Fig. 14 Typical comparison of experimental and numerical stress–strain curves for sandstone specimens containing two non-coplanar fissures under uniaxial compression

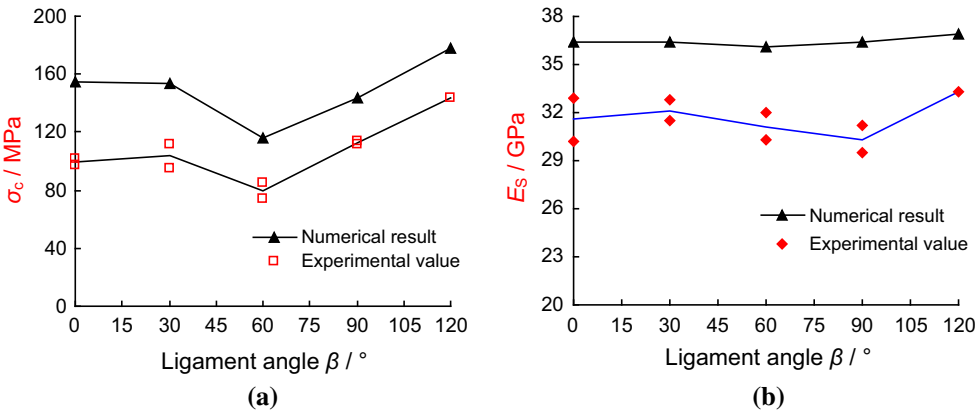

Fig. 15 Comparison of experimental and numerical mechanical parameters for brittle sandstone specimens containing two non-coplanar fissures under uniaxial compression

many circular particles, which cannot exactly simulate the 3-D experimental specimen (Lee and Jeon 2011). On the other hand, it is possibly the influence of the heterogeneity of the tested rock material or inherent randomness of the numerical simulation.

4.3 Analysis of Crack Evolution Mechanism

Figure 16 illustrates the influence of ligament angle β on the ultimate failure mode of brittle sandstone specimens containing two non-coplanar fissures under uniaxial compression using PFC^{2D} numerical simulation. In Fig. 16, the black points stand for the tensile crack, while the blue points stand for the shear crack. In accordance with the comparison with the experimental ultimate failure mode (see Fig. 7), we can see that the PFC^{2D} software can be used to simulate the cracking characteristics of brittle sandstone material. The ultimate failure modes of numerical specimens show good agreement with those of experimental specimens.

In order to analyze the crack evolution mechanism of brittle sandstone containing two non-coplanar fissures under uniaxial compression, we take the specimen for $\beta = 90°$ as an example, as shown in Figs. 17 and 18. The letters in Fig. 17 correspond to those shown in Fig. 18. From Fig. 17, we can see that the tensile cracks in the specimen are considerably greater in number than the shear cracks, and the differences are more obvious with the increase of axial deformation. For each numerical specimen, more crack numbers occur after the peak strength and tensile cracks increase exponentially with the increase of axial deformation. Moreover, the increasing rate of tensile crack numbers after the peak strength is obviously higher than that before the peak strength.

Figure 18 illustrates the crack evolution process and the force fields of brittle sandstone specimens containing two non-coplanar fissures ($\beta = 90°$). In the orange images of Fig. 18, the black points stand for the tensile crack, while the blue points stand for the shear crack. In Fig. 18, the black images are the distribution of contact force. The red lines

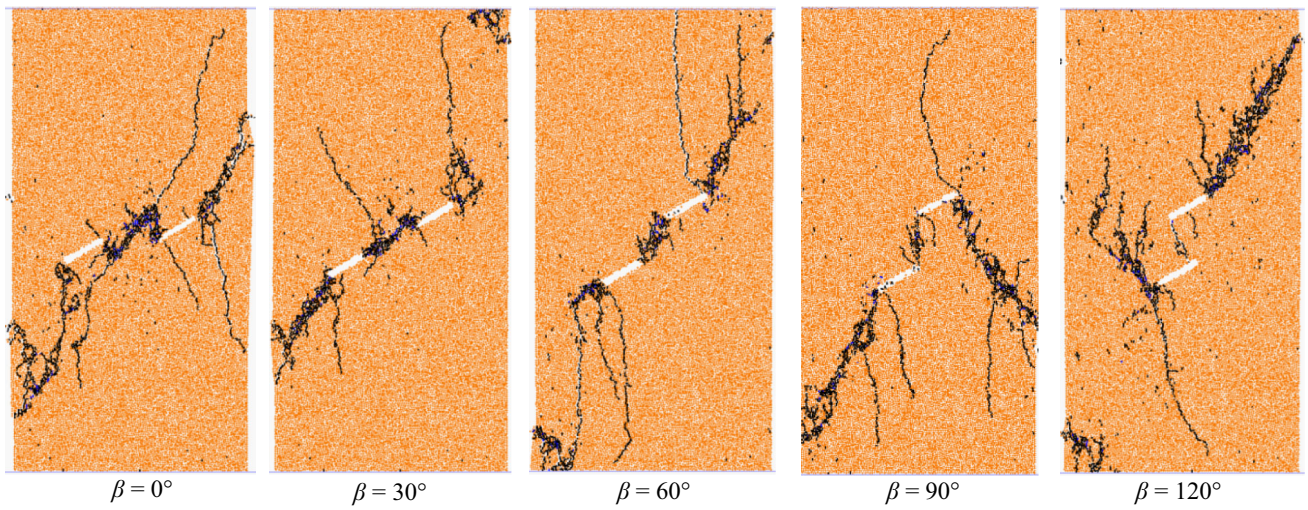

Fig. 16 Numerical results of ultimate failure modes of brittle sandstone specimens containing two non-coplanar fissures under uniaxial compression

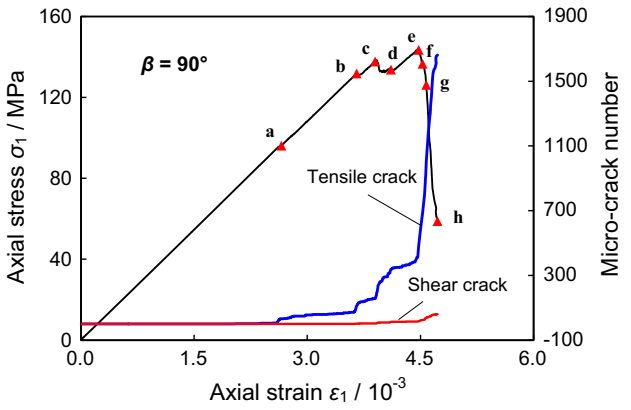

Fig. 17 Relation between axial stress–axial strain curve and micro-crack numbers of brittle sandstone ($\beta = 90°$)

stand for the crack, while the black lines stand for contact force. However, the blue images of Fig. 18 are the distribution of parallel bond force, which is represented by the discrete straight line segments. Red color stands for tensile force, while blue color stands for compressive force. Line thickness and orientation correspond to force magnitude and direction, respectively. When the specimen was loaded to point *a* (67.5 % σ_c), tensile wing crack 1 was initiated from the tips of two pre-existing fissures. At this time, the maximum contact force and the maximum parallel bond force were, respectively, 198 and 99.8 kN. When crack 1 was initiated, the tensile stress concentration in this region was released, shown by the numerous red colors at the tips of the tensile wing crack in the parallel bond force field.

As the axial stress was increased to point *b* (91.9 % σ_c), tensile wing crack 1 appeared to propagate along the direction of axial stress, but, at the same time, a new secondary tensile crack 2 was initiated from the inner tip of fissure ② and propagated in the upper direction, but did not reach the inner tip of fissure ①. From point *a*, the red color was crowded in the ligament region, indicating the initiation of secondary tensile crack 2 at point *b*. At point *b*, the maximum contact force and the maximum parallel bond force were, respectively, 272 and 178 kN.

With the increase of axial deformation, when the specimen was loaded to point *c* (95.4 % σ_c), the specimen underwent coalescence failure in the ligament region, i.e., crack 3 emanated between the inner tips of two pre-existing fissures. After crack 3 was initiated, the compressive and tensile stress concentrations in the ligament region were all released, as indicated by the increased blank areas compared with point *b*. It should be noted that, due to the interaction of force fields in the ligament region, tensile cracks 1^c and 1^d had difficulty propagating further along the direction of axial stress. At point *c*, the maximum contact force and the maximum parallel bond forces were 319 and 162 kN, respectively.

Fig. 18 Crack evolution process and force field of brittle sandstone specimens containing two non-coplanar fissures ($\beta = 90°$). The *black images* show the distribution of contact force. The *blue images* show the distribution of parallel bond force. **a** Point *a*, $\sigma_1 = 96.92$ MPa, $\varepsilon_1 = 2.679 \times 10^{-3}$, (**b**) point *b*, $\sigma_1 = 131.88$ MPa, $\varepsilon_1 = 3.656 \times 10^{-3}$, (**c**) point *c*, $\sigma_1 = 136.97$ MPa, $\varepsilon_1 = 3.933 \times 10^{-3}$, (**d**) point *d*, $\sigma_1 = 134.17$ MPa, $\varepsilon_1 = 4.172 \times 10^{-3}$, (**e**) point *e*, $\sigma_1 = 143.53$ MPa = peak value, $\varepsilon_1 = 4.475 \times 10^{-3}$, (**f**) point *f*, $\sigma_1 = 136.63$ MPa, $\varepsilon_1 = 4.529 \times 10^{-3}$, (**g**) point *g*, $\sigma_1 = 131.17$ MPa, $\varepsilon_1 = 4.566 \times 10^{-3}$, (**h**) point *h*, $\sigma_1 = 58.85$ MPa, $\varepsilon_1 = 4.726 \times 10^{-3}$

The continuous increase of axial deformation led to the specimen being loaded to point *d*. At this time, although the axial strain increased from 3.933×10^{-3} at point *c* to 4.172×10^{-3} at point *d*, the axial stress had a small stress drop, decreasing from 136.97 to 134.17 MPa, as a result of the propagation of tensile wing cracks 1^a and 1^b along the direction of axial stress. In the ligament region, although the cracks did not change, the force field varied greatly, and more blank areas were observed compared than at point *c*. Furthermore, compared with the parallel bond force field near cracks 1^a and 1^b from point *a* to *d*, at the tips of newly developed cracks, the red color increased greatly, as shown in the elliptical region, which meant that the newly developed crack tips would serve as the new tensile stress concentration region. Compared with that at point *c*, the maximum contact force increased further to 418 kN from 319 kN. However, the maximum parallel bond force decreased further to 147 kN from 162 kN.

After point *d*, the continuous increase of axial deformation led to the specimen being loaded to peak strength point *e* (100 % σ_c). One new anti-tensile crack 4 was initiated from the outer tip of fissure ① and propagated in the downward direction. Moreover, tensile wing cracks 1^a and 1^b also propagated a little along the direction of axial stress. At this time, the maximum contact force decreased from 418 to 390 kN, whereas the parallel bond force increased greatly from 147 to 171 kN. It should be noted that more tensile force concentrations at point *e* were released than at point *d* due to the emanation of crack 4. However, in the ligament region, the force field did not vary.

After peak strength (point *e*), with the increase of axial deformation, the axial stress began to reduce. When the axial stress was reduced to point *f* ($\sigma_1 = 136.63$ MPa, $\varepsilon_1 = 4.529 \times 10^{-3}$), crack 4 propagated towards the bottom edge of the specimen along the direction of axial stress. Due to the propagation of crack 4, more blank areas were found near crack 4. At point *f*, the maximum contact force and the maximum parallel bond force were 655 kN and 174 kN, respectively. Compared with that at peak strength, the maximum contact force at point *f* increased significantly, but the maximum parallel bond force remained basically constant. The increase of axial deformation led to the specimen being loaded to point

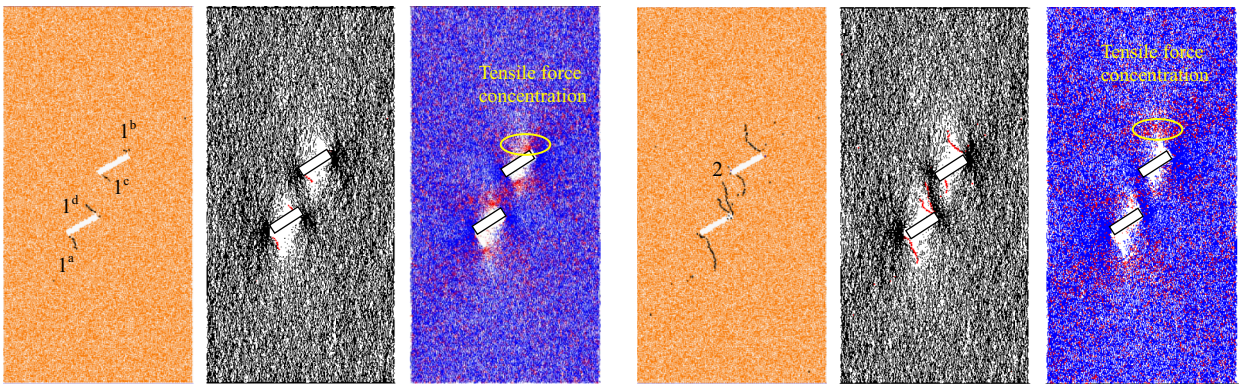

(a) Point a, σ_1=96.92 MPa, ε_1=2.679×10^{-3} **(b)** Point b, σ_1=131.88 MPa, ε_1=3.656×10^{-3}

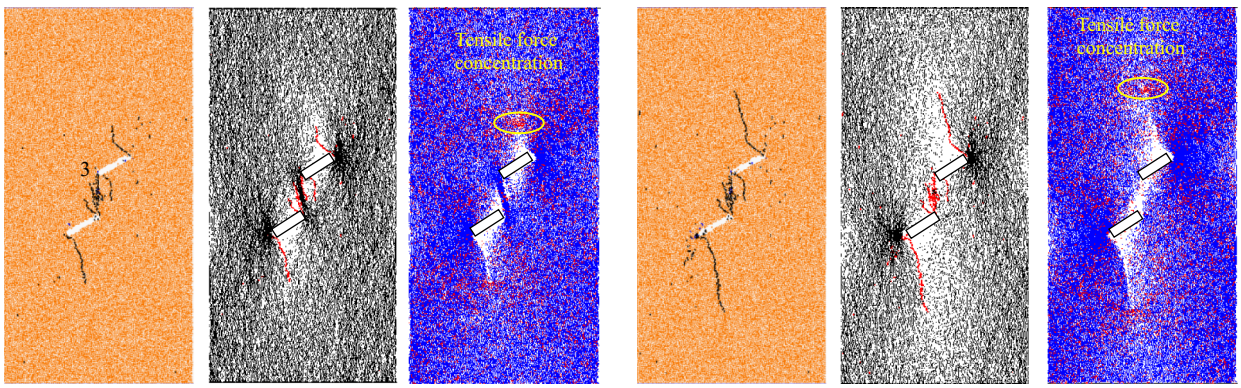

(c) Point c, σ_1=136.97 MPa, ε_1=3.933×10^{-3} **(d)** Point d, σ_1=134.17 MPa, ε_1=4.172×10

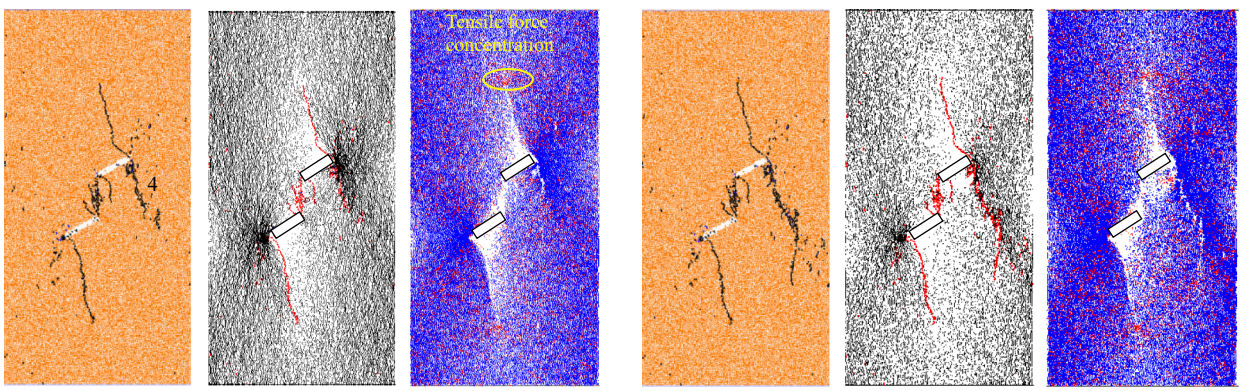

(e) Point e, σ_1=143.53 MPa= Peak value, ε_1=4.475×10^{-3} **(f)** Point f, σ_1=136.63 MPa, ε_1=4.529×10^{-3}

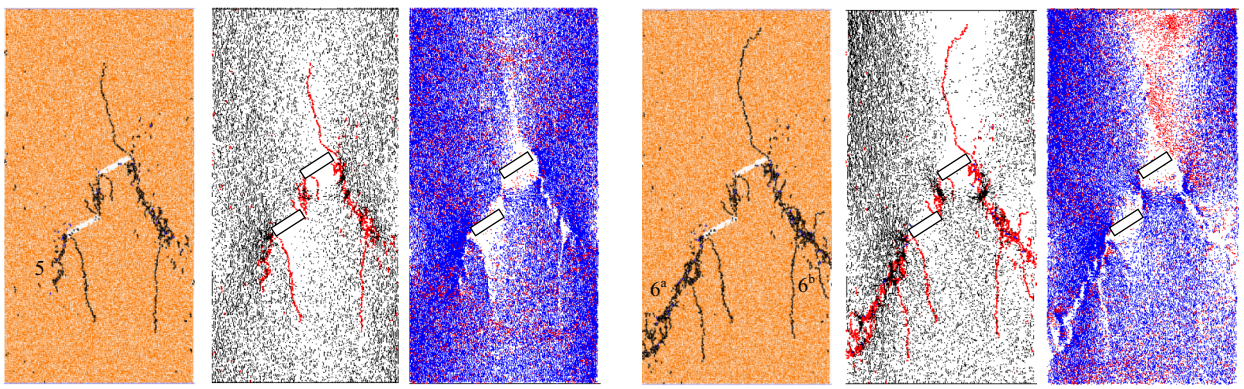

(g) Point g, σ_1=131.17 MPa, ε_1=4.566×10^{-3} **(h)** Point h, σ_1=58.85 MPa, ε_1=4.726×10^{-3}

g ($\sigma_1 = 131.17$ MPa, $\varepsilon_1 = 4.566 \times 10^{-3}$). At this time, crack 4 further propagated towards the bottom edge of the specimen along the direction of axial stress. Secondary tensile crack 5 was initiated from the outer tip of fissure ② and propagated in the downward direction. The maximum contact force reached 789 kN, but the maximum parallel bond force decreased slightly from 174 to 171 kN. More tensile force concentrations were released due to the propagation of cracks 4 and 5.

When the axial stress was decreased to point h ($\sigma_1 = 58.85$ MPa, $\varepsilon_1 = 4.726 \times 10^{-3}$), two new cracks ($6^a$ and 6^b) were initiated, and original cracks 1^b and 5 propagated towards the edges of the specimen along the direction of axial stress. At this time, the specimen failed completely in the final macroscopic failure mode. The maximum contact force decreased rapidly from 789 to 361 kN and the maximum parallel bond force from 171 to 147 kN, as a result of the release of force concentration in the specimen. It should be noted that, when the macroscopic crack was initiated, many blank areas in the parallel bond force field were also observed.

Figure 19 illustrates the influence of ligament angle on the micro-crack number evolution curves of brittle sandstone specimens containing two non-coplanar fissures under uniaxial compression. For comparison, the micro-crack number evolution curve of an intact specimen is also plotted in Fig. 19. From Fig. 19, it can be seen that, with the increase of axial deformation, the micro-crack numbers first increase slowly, and then increase rapidly until failure for the same ligament angle. The evolving rate of micro-crack numbers of the intact specimen is higher than that of the fissured specimens, but depends on the ligament angle. It should be noted that, in all cases, the evolving rate of micro-crack numbers of the fissured specimen for $\beta = 60°$ is lowest, whereas the evolving rate of micro-crack numbers of the fissured specimen for $\beta = 120°$ is highest. However, the evolving rate of micro-crack numbers for the fissured specimen for $\beta = 0°$ is approximately equal to that for $\beta = 30°$. Generally, the dependence of the micro-crack evolving rate on the ligament angle corresponds to that of uniaxial compressive strength. The failure under higher stress accompanied by the release of higher accumulated strain energy will be more violent and cause a higher micro-crack evolving rate.

5 Conclusions

In this research, the influence of ligament angle on the strength, deformability, and crack evolution behavior of rectangular prismatic specimens (80 × 160 × 30 mm) of brittle sandstone containing two non-coplanar fissures under uniaxial compression was evaluated by experiment and discrete element modeling. Based on these experimental and numerical results, the following conclusions can be drawn.

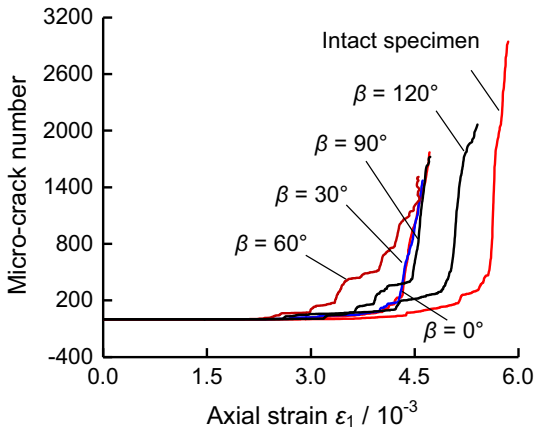

Fig. 19 Micro-crack number evolution curve of brittle sandstone specimens containing two non-coplanar fissures

Tested intact sandstone is a typical brittle rock which undergoes axial splitting failure. The experimental results show that the peak strength and elastic modulus of sandstone specimens containing two non-coplanar fissures are all lower than that of intact specimens, but the extent of reduction is related to the ligament angle. The elastic modulus of flawed specimens is not obviously related to the ligament angle, although it is a little lower than that of intact specimens. With the increase of ligament angle, the peak strength decreases at a ligament angle of 60°, before increasing up to our maximum ligament angle of 120°.

Crack initiation, propagation, and coalescence are all observed and characterized from the inner and outer tips of pre-existing non-coplanar fissures in brittle sandstone using photographic monitoring. Based on the results, the sequence of crack evolution in sandstone containing two non-coplanar fissures is analyzed in detail on the basis of the crack propagation mechanism (tensile, shear, lateral crack, far-field crack, and surface spalling). The macroscopic failure modes of sandstone specimens containing two non-coplanar fissures are all a mixture of several cracks.

In order to understand the crack evolution mechanism of brittle sandstone, numerical simulation by PFC^{2D} was performed for specimens containing two non-coplanar fissures. Numerically simulated results for sandstone specimen containing two non-coplanar fissures under uniaxial compression show good agreement with the experimental results. By the analysis of the force field, the crack evolution mechanism in brittle sandstone containing two non-coplanar fissures under uniaxial compression is revealed. These experimental and numerical results are expected to improve the understanding of the unstable fracture mechanism of fissured rock engineering structures.

Acknowledgments This research was supported by the Program for New Century Excellent Talents in University (NCET-12-0961), the National Natural Science Foundation of China (51179189), the Fundamental Research Funds for the Central Universities (China University of Mining and Technology) (2014YC10), the Outstanding Innovation Team Project in China University of Mining and Technology (2014QN002), the Team Project Funded by 2014 Jiangsu Innovation and Entrepreneurship Program, and Natural Science Foundation of Jiangsu Province for Distinguished Young Scholars (BK20150005). The authors would also like to express their sincere gratitude to the editor, Giovani Barla, and the anonymous reviewers for their valuable comments, which have greatly improved this paper.

References

Behbahani SS, Moarefvand P, Ahangari K, Goshtasbi K (2013) Unloading scheme of Angooran mine slope by discrete element modeling. Int J Rock Mech Min Sci 64:220–227

Chen CS, Pan E, Amadei B (1998) Fracture mechanics analysis of cracked discs of anisotropic rock using the boundary element method. Int J Rock Mech Min Sci 35(2):195–218

Cho N, Martin CD, Sego DC (2007) A clumped particle model for rock. Int J Rock Mech Min Sci 44(7):997–1010

Colombo D, Massin P (2011) Fast and robust level set update for 3D non-planar X-FEM crack propagation modelling. Comput Methods Appl Mech Eng 200(25–28):2160–2180

Debecker B, Vervoort A (2009) Experimental observation of fracture patterns in layered slate. Int J Fract 159:51–62

Debecker B, Vervoort A (2013) Two-dimensional discrete element simulations of the fracture behaviour of slate. Int J Rock Mech Min Sci 61:161–170

Esterhuizen GS, Dolinar DR, Ellenberger JL (2011) Pillar strength in underground stone mines in the United States. Int J Rock Mech Min Sci 48:42–50

Feng XT, Pan PZ, Zhou H (2006) Simulation of the rock microfracturing process under uniaxial compression using an elasto-plastic cellular automaton. Int J Rock Mech Min Sci 43(7):1091–1108

Feng XT, Ding WX, Zhang DX (2009) Multi-crack interaction in limestone subject to stress and flow of chemical solutions. Int J Rock Mech Min Sci 46(1):159–171

Grégoire D, Maigre H, Rethore J, Combescure A (2007) Dynamic crack propagation under mixed-mode loading—comparison between experiments and X-FEM simulations. Int J Solid Struct 44(20):6517–6534

Hall SA, De Sanctis F, Viggiani G (2006) Monitoring fracture propagation in a soft rock (Neapolitan Tuff) using acoustic emissions and digital images. Pure Appl Geophys 163:2171–2204

Janeiro RP, Einstein HH (2010) Experimental study of the cracking behavior of specimens containing inclusions (under uniaxial compression). Int J Fract 164(1):83–102

Jia LC, Chen M, Zhang W, Xu T, Zhou Y, Hou B, Jin Y (2013) Experimental study and numerical modeling of brittle fracture of carbonate rock under uniaxial compression. Mech Res Commun 50:58–62

Lee H, Jeon S (2011) An experimental and numerical study of fracture coalescence in pre-cracked specimens under uniaxial compression. Int J Solids Struct 48(6):979–999

Li YP, Chen LZ, Wang YH (2005) Experimental research on pre-cracked marble under compression. Int J Solids Struct 42:2505–2516

Li XB, Zou Y, Zhou ZL (2014) Numerical simulation of the rock SHPB test with a special shape striker based on the discrete element method. Rock Mech Rock Eng 47(5):1693–1709

Mughieda O, Omar MT (2008) Stress analysis for rock mass failure with offset joints. Geotech Geol Eng 26:543–552

Pan PZ, Feng XT, Hudson JA (2009) Study of failure and scale effects in rocks under uniaxial compression using 3D cellular automata. Int J Rock Mech Min Sci 46(4):674–685

Park CH, Bobet A (2009) Crack coalescence in specimens with open and closed flaws: a comparison. Int J Rock Mech Min Sci 46(5):819–829

Potyondy DO, Cundall PA (2004) A bonded-particle model for rock. Int J Rock Mech Min Sci 41(8):1329–1364

Prudencio M, Van Sint Jan M (2007) Strength and failure modes of rock mass models with non-persistent joints. Int J Rock Mech Min Sci 44(6):890–902

Rozycki P, Moës N, Bechet E, Dubois C (2008) X-FEM explicit dynamics for constant strain elements to alleviate mesh constraints on internal or external boundaries. Comput Methods Appl Mech Eng 197(5):349–363

Shen B (1995) The mechanism of fracture coalescence in compression—experimental study and numerical simulation. Eng Frac Mech 51(1):73–85

Shen B, Stephansson O (1993) Numerical analysis of mixed mode I and mode II fracture propagation. Int J Rock Mech Min Sci Geomech Abst 30(7):861–867

Tang C (1997) Numerical simulation of progressive rock failure and associated seismicity. Int J Rock Mech Min Sci 34(2):249–261

Tang CA, Kou SQ (1998) Crack propagation and coalescence in brittle materials under compression. Eng Fract Mech 61:311–324

Tang CA, Chen ZH, Xu XH, Li C (1997) A theoretical model for Kaiser effect in rock. Pure Appl Geophys 150(2):203–215

Tang CA, Tham LG, Lee PKK, Tsui Y, Liu H (2000) Numerical studies of the influence of microstructure on rock failure in uniaxial compression—part II: constraint, slenderness and size effect. Int J Rock Mech Min Sci 37(4):571–583

Vásárhelyi B, Bobet A (2000) Modeling of crack initiation, propagation and coalescence in uniaxial compression. Rock Mech Rock Eng 33(2):119–139

Wong LNY, Einstein HH (2009) Crack coalescence in molded gypsum and Carrara marble: part 1. Macroscopic observations and interpretation. Rock Mech Rock Eng 42(3):475–511

Wong RHC, Tang CA, Chau KT, Lin P (2002) Splitting failure in brittle rocks containing pre-existing flaws under uniaxial compression. Eng Fract Mech 69:1853–1871

Xu T, Tang CA, Yang TH, Zhu WC, Liu J (2006) Numerical investigation of coal and gas outbursts in underground collieries. Int J Rock Mech Min Sci 43(6):905–919

Yang SQ (2011) Crack coalescence behavior of brittle sandstone samples containing two coplanar fissures in the process of deformation failure. Eng Frac Mech 78(17):3059–3081

Yang SQ, Huang YH (2014) Particle flow study on strength and meso-mechanism of Brazilian splitting test for jointed rock mass. Acta Mech Sinica 30(4):547–558

Yang SQ, Jing HW (2011) Strength failure and crack coalescence behavior of brittle sandstone samples containing a single fissure under uniaxial compression. Int J Fract 168(2):227–250

Yang SQ, Yang DS, Jing HW, Li YH, Wang SY (2012) An experimental study of the fracture coalescence behaviour of brittle sandstone specimens containing three fissures. Rock Mech Rock Eng 45(4):563–582

Yang SQ, Huang YH, Jing HW, Liu XR (2014) Discrete element modeling on fracture coalescence behavior of red sandstone containing two unparallel fissures under uniaxial compression. Eng Geol 178:28–48

Zhang XP, Wong LNY (2012) Cracking processes in rock-like material containing a single flaw under uniaxial compression: a numerical study based on parallel bonded-particle model approach. Rock Mech Rock Eng 45:711–737

Zhang XP, Wong LNY (2013) Loading rate effects on cracking behavior of flaw-contained specimens under uniaxial compression. Int J Fract 180:93–110